

A rock-physics investigation of unconsolidated saline permafrost: P-wave properties from laboratory ultrasonic measurements

Shan Dou¹, Seiji Nakagawa², Douglas Dreger³, and Jonathan Ajo-Franklin²

ABSTRACT

Saline permafrost is sensitive to thermal disturbances and is prone to subsidence, which renders it a major source of geohazard in Arctic coastal environments. Seismic methods could be used to map and monitor saline permafrost at scales of geotechnical interests because of the ice-content dependencies of seismic properties. We have developed a comprehensive study of the ultrasonic P-wave properties (i.e., velocity and attenuation) of synthetic saline permafrost samples for a range of salinities and temperatures, and measurements conducted on a fine-grained permafrost core obtained from Barrow, Alaska. The resulting data consist of P-wave properties presented as functions of temperature and salinity. Notable observations include the following: P-wave velocities showed marked reductions in the presence of dissolved salts and complex variations

resulting from the water-to-ice phase transitions; strong P-wave attenuation was present in the temperature intervals in which the samples were partially frozen. When presented as functions of ice saturation, the data sets lead us to two key findings: (1) neither a purely cementing nor a purely pore-filling model of the pore-scale distributions of ice could adequately fit the observed velocity data and (2) although the velocities increase monotonically with increasing ice saturations, P-wave attenuation reaches a maximum at intermediate ice saturations — contrary to the ordinary expectation of decreasing attenuation with increasing velocities. The observed ice-content dependencies of P-wave properties, along with the implications on the probable pore-scale distributions of ice, provide a valuable basis for rock-physics modeling, which in turn could facilitate seismic characterizations of saline permafrost.

INTRODUCTION

Saline permafrost is widespread in subsea and coastal areas of the Arctic, in which marine deposits and/or seawater incursions provide a source for dissolved salts (Osterkamp, 1989; Hivon and Sego, 1993; Brouchkov, 2002, 2003; Ingeman-Nielsen et al., 2008). Due to freezing-point depression of the saline pore water, saline permafrost is not fully frozen when temperatures are above the eutectic point (approximately -21°C for NaCl solution). Given that the Arctic ground temperatures rarely fall below the eutectic point, natural saline permafrost is typically only partially frozen.

As a system in which water and ice coexist in a delicate phase equilibrium, partially frozen saline permafrost is highly sensitive to temperature disturbances. Unlike nonsaline permafrost that is

largely stable at subzero temperatures, saline permafrost can begin thawing at temperatures that are well less than 0°C . Thus, in a warming climate, saline permafrost is likely to degrade at an accelerated pace. Moreover, saline permafrost is mechanically weaker because less ice is available for bonding the sediment grains together. Consequently, infrastructure built on saline permafrost is prone to damage and failure (e.g., Ogata et al., 1983; Nixon and Lem, 1984; Hivon and Sego, 1995). For instance, Brouchkov (2003) reports that 25%–50% of the buildings along the Russian Arctic coast have deformed because of the underlying saline permafrost.

Given the profound influences of saline permafrost, knowledge about its distribution is crucial. Seismic methods can be useful for mapping saline permafrost at spatial scales of geotechnical interest

Manuscript received by the Editor 15 March 2015; revised manuscript received 24 August 2015; published online 29 January 2016.

¹Formerly University of California, Berkeley, Department of Earth and Planetary Science, Berkeley, California, USA; presently Lawrence Berkeley National Laboratory, Earth and Environmental Sciences Area, Energy Geosciences Division, Berkeley, California, USA. E-mail: shandou.seismo@gmail.com.

²Lawrence Berkeley National Laboratory, Earth and Environmental Sciences Area, Energy Geosciences Division, Berkeley, California, USA. E-mail: snakagawa@lbl.gov; jbajo-franklin@lbl.gov.

³University of California, Berkeley, Department of Earth and Planetary Science, Berkeley, California, USA. E-mail: ddreger@berkeley.edu.

© 2016 Society of Exploration Geophysicists. All rights reserved.

(tens to hundreds of meters laterally and vertically). Among the seismic properties typically evaluated, seismic velocities are used most often in permafrost studies (e.g., Miller et al., 2000; Hilbich, 2010; Ramachandran et al., 2011). Key to this application is the positive correlation between the ice content and seismic velocities: In general, the higher the ice content, the higher the velocities (e.g., Timur, 1968; Nakano and Arnold, 1973; Zimmerman and King, 1986). Moreover, seismic velocities are relevant to engineering practices because correlations often exist between velocities and strength of geomaterials (Schön, 2011). Besides velocities, seismic attenuation (e.g., Q values) is also sensitive to the ice content (e.g., Nakano and Arnold, 1973; Matsushima et al., 2011a, 2011b) and thus may also be useful for detecting and delineating permafrost.

For mapping and characterizing saline permafrost, the ice-content dependencies of seismic properties are particularly useful. Because saline permafrost contains less ice, it is readily identifiable as a low-velocity anomaly within a high-velocity background of non-saline permafrost (Collett and Bird, 1988, 1993; Schmitt et al., 2005; Dou and Ajo-Franklin, 2014). However, identifying saline permafrost only constitutes part of the task. Often, the next step is to estimate its ice content. Because ice plays critical roles in maintaining the integrity and stability of the frozen ground, the ice-content estimates are key for risk assessment concerning permafrost degradation. To deduce ice content from seismic measurements, one must use rock-physics models that quantitatively relate seismic measurements to ice content. Such models should be established based on data that are associated with a wide range of ice content. Laboratory experiments can provide data for this purpose, given that controlled conditions can be used to produce a variety of ice content.

Unfortunately, few previous studies have probed the seismic properties of unconsolidated saline permafrost. Prior studies have largely focused on consolidated sedimentary rocks (Desai and Moore, 1967; Pandit and King, 1978, 1979; Sondergeld and Rai, 2007), whereas predominant portions of the near-surface saline permafrost units consist of unconsolidated sediments. To date, we have only found two published laboratory studies that address the influences of pore-water salinity on unconsolidated frozen sediments: King et al. (1982) conduct measurements on subsea perma-

frost samples, and Matsushima et al. (2011a) explore the properties of brine-saturated quartz sand. However, because only limited ranges of temperatures and salinities were tested, the data produced by these studies are insufficient for constructing rock-physics models of unconsolidated saline permafrost.

In this study, we conducted laboratory ultrasonic measurements to investigate P-wave properties of saturated, unconsolidated saline permafrost over wide ranges of salinities and temperatures. We used coarse-grained sand packs saturated with water or NaCl solutions of various concentrations (0.0–2.5 M; 0–130 ppt) to systematically examine the influences of pore-water salinities. We also carried out measurements on a fine-grained saline permafrost core sample (0.7 M; 42 ppt) to appraise the influences of surface effects (i.e., capillary effect of small pores and adsorption effect of mineral surfaces). Each set of measurements covers a broad temperature range from 10°C to –30°C.

Lastly, we analyze the observed P-wave properties of the sand samples as functions of ice content, from which we deduce constraints on the pore-scale distribution of ice. The data set and the associated realizations of the pore-scale structures provide valuable bases for rock-physics modeling, which could ultimately facilitate seismic characterizations of saline permafrost.

BACKGROUND

So far our discussion has been centered on the relationship between seismic properties and ice content. However, we cannot speak solely about the variations of ice content without mentioning the complementary variations in the unfrozen water content. In the context of this paper, we define unfrozen water as water (saline or nonsaline) that remains liquid at subzero temperatures.

The presence of unfrozen water is pivotal to seismic properties of saline permafrost. To facilitate the data interpretation later on, we provide a brief background on mechanisms that prevent unfrozen water from freezing, and the plausible causes of freeze-thaw hysteresis.

Mechanisms for unfrozen water to remain liquid below freezing

Freezing-point depression

The determining factor that distinguishes saline permafrost from its nonsaline counterpart is the pronounced freezing-point depression caused by dissolved salts. Besides salts, other causes of freezing-point depression are surface effects such as the capillary effect of small pores and the adsorption of mineral surfaces. Here, we provide a brief explanation of these causes:

- 1) Dissolved salts: Dissolved salts make water molecules in a solution more disordered than those in pure water. Consequently, lower temperatures are required to transform these more disordered molecules into structurally organized ice crystals. The higher is the concentration of the salts, the lower is the freezing point. We note that the freezing point has a lower limit known as the eutectic point (defined as the lowest temperature in which a solution can remain liquid). Once the temperature falls below the eutectic point, all the dissolved salts precipitate out of the solution as salt crystals regardless of the salt concentration, and the residual water rapidly freezes (Figure 1). Between the freezing point and the eutectic point, ice and salty water coexist,

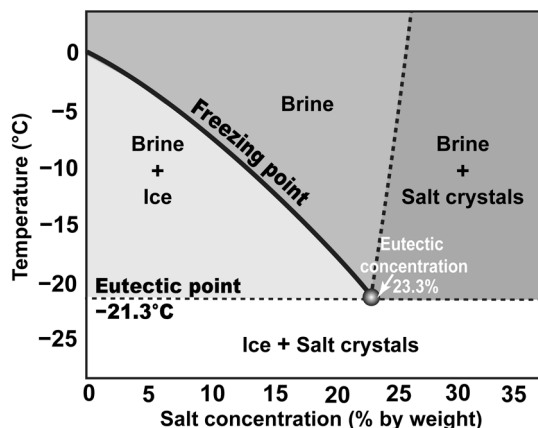


Figure 1. Phase diagram of NaCl-H₂O binary system. The eutectic point (–21.3°C) is the lowest temperature in which this binary system can contain liquid. It also is the freezing point of the solution with the eutectic concentration (23.3 wt%; 233 ppt).

yielding a partially frozen “slurry.” When cooling occurs within this temperature range, the solution experiences progressive freezing: That is, as freezing occurs in response to a decrease in temperature, the newly formed ice lattices cannot tolerate impurities and thus reject the salts into the residual solution; because the more concentrated residual solution has a lower freezing point, freezing quickly comes to a stop unless the temperature decreases further.

2) Surface effects

- **Capillary effect:** We consider the freezing of water confined in capillary pores (i.e., small pores and narrow pore throats). To simplify the explanation, we use a capillary tube with an inner radius as an analog of the pore space. For hydrophilic sediments that undergo freezing, water is the wetting phase and ice is the nonwetting phase. At the ice-water interface, capillary pressure is present and acts as an excess pressure that lowers the freezing point (Blachere and Young, 1972; Fagerlund, 1973; Hall and Hoff, 2012) (Figure 2a). The Young-Laplace equation of capillarity indicates that smaller capillary pores yield higher excess pressures and as a result, lower freezing points.
- **Adsorption:** Water molecules are highly dipolar. Due to the electrostatic attraction between charges of opposite polarities, water molecules can be adsorbed onto electrically charged mineral surfaces (e.g., clay minerals) (Figure 2b). The adsorption effect is of a very short range, forming a thin water layer that usually is a few molecules thick. Hence, the adsorbed water only comprises a small fraction of the total water content. This small amount of water, however, is often considered “unfreezable” because of its strong resistance to freezing (e.g., Fagerlund, 1973; Kozłowski and Nartowska, 2013).

Supercooling

Supercooling of a liquid is the maintenance of its liquid state below the freezing point. For porous sediments, supercooling mainly affects the free water (Andersland and Ladanyi, 2004). Supercooled water is metastable. If the temperature gets low enough, or if ice microparticles grow sufficiently large to facilitate nucleation, the supercooled water freezes spontaneously and rapidly. The temper-

ature in which the supercooled water starts to freeze is called the supercooling point (Zachariassen, 2005).

We note that supercooling and freezing-point depression are inherently different. Whereas freezing-point depression is deterministic by nature and the depressed freezing point often can be predicted, supercooling is a stochastic process, and a precise prediction of the supercooling point is impossible (Setzer, 1997; Wilson et al., 2003). Thus, supercooled water can have a range of supercooling points but only one freezing point. This is also reflected in one common observation that when a supercooled sample starts to freeze, its temperature rises quickly and then remains close to the freezing point. Such temperature compensation results from the latent heat of fusion that is released upon the formation of ice (Davis, 2001; Andersland and Ladanyi, 2004) (Figure 3).

Plausible causes of freeze-thaw hysteresis

In the phase transition processes, hysteresis is often observed, for example, the condensation-evaporation hysteresis of CO₂ reported by Kofman et al. (2013) and the growth-dissociation hysteresis of gas hydrate reported by Anderson et al. (2009). Freeze-thaw processes in permafrost are no exception. There are at least two plausible causes of freeze-thaw hysteresis:

- **Capillary hysteresis:** If pore sizes and shapes are noticeably nonuniform, the pore spaces can be represented with large spherical pores interconnected by thin capillary tubes. Analogous to the familiar phenomenon of the drainage-imbibition hysteresis concerning ice-free sediments, the macroscopic manifestation of a freeze-thaw hysteresis can be explained by the microscopic mechanism of the “ink-bottle” effect (Figure 4): The capillary pressure of thawing ($P_{\text{capillary}}^{\text{[thaw]}}$, analogous to $P_{\text{capillary}}^{\text{[imb]}}$) is governed by the radius of the large pores (bottle reservoir), whereas the capillary pressure of freezing ($P_{\text{capillary}}^{\text{[freeze]}}$, analogous to $P_{\text{capillary}}^{\text{[drain]}}$) is governed by the radius of the capillary tubes. As a result, $P_{\text{capillary}}^{\text{[freeze]}}$ is higher than $P_{\text{capillary}}^{\text{[thaw]}}$ and the extent of the freezing-/melting-point depression scales accordingly, yielding a freeze-thaw hysteresis (Spaans and Baker, 1996; Bittelli et al., 2003).
- **Supercooling:** As described earlier, once a supercooled sample starts to freeze, its temperature often rises back to the freezing point due to the latent heat of fusion (as shown in Figure 3). In this case, supercooling renders a hysteresis loop of zero area. However, if for any reason the amount of

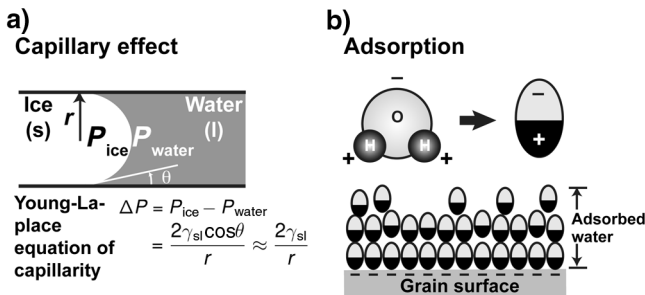


Figure 2. Schematics of surface effects: (a) capillary effect of small pores or narrow pore throats (γ_{sl} , surface tension at the solid-liquid interface; θ , contact angle; r , inner radius of the capillary tube) and (b) adsorption effect of mineral surfaces.

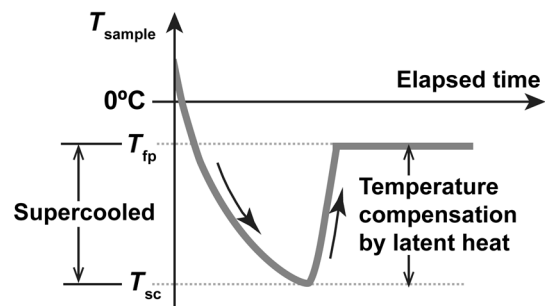


Figure 3. Schematic cooling curve of pore water close to onset of freezing; T_{fp} , freezing point and T_{sc} , supercooling point.

the latent heat is insufficient to fully compensate the temperature difference between the freezing point and the supercooling point, a discernible freeze-thaw hysteresis can appear.

EXPERIMENTAL SYSTEM, MATERIALS, AND PROCEDURE

Ultrasonic pulse-transmission system

An ultrasonic pulse-transmission system was used for our laboratory experiments (Figure 5). An upright cylindrical acrylic column (internal diameter, 65.3 mm and height, 150 mm) functioned both as a sample container and a mounting frame for ultrasonic and temperature sensors. Two levels of instrument ports were

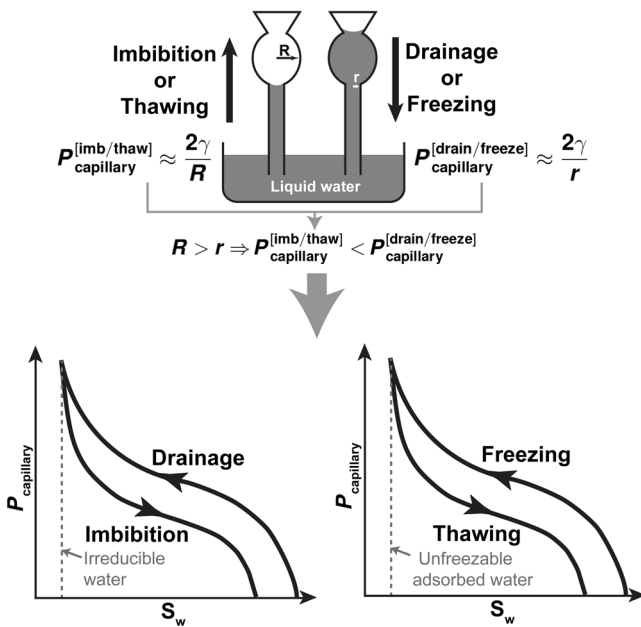


Figure 4. Schematics of capillary hysteresis and the ink-bottle effect.

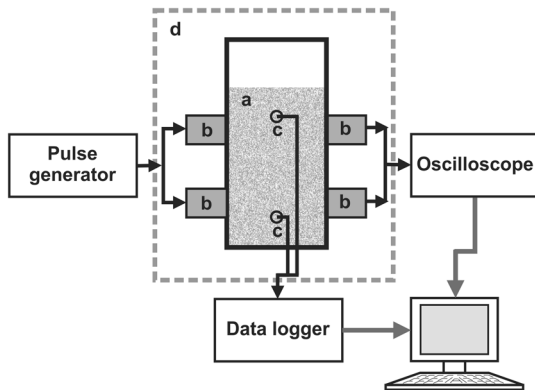


Figure 5. Schematics of the ultrasonic pulse-transmission system. a, sample column; b, ultrasonic transducers; c, thermocouples; and d, benchtop freezer.

attached to the sidewall of the column at heights of 42 and 73 mm (relative to the base of the column). Each level consisted of two ultrasonic transducer ports and one thermocouple port. The two transducer ports, one for the transmitter and the other for the receiver, were positioned at opposite sides about the symmetry axis of the column, so that the acquired signals were P-waves propagating along the diameter direction of the cylindrical sample; the thermocouple port, through which a thermocouple probe was inserted into the sample, was placed 90° away from the transducer ports.

A square-wave pulse generator (Panametrics 5077PR) was used to provide high-voltage (100–400 V), high-frequency (central frequency 1 MHz) excitation signals for the ultrasonic transducers. To achieve good acoustic coupling between the transducers and the saturated samples, immersion-type transducers (central frequency, 1 MHz; Panametrics V303-SU) were used for transmitting and receiving ultrasonic signals. The through-transmission ultrasonic signals were acquired using a digital oscilloscope (Tektronix TDS 210) and saved on a control PC for analysis.

Experimental materials

As mentioned earlier (see the “Background” section), pore-water salinities and surface effects both influence ice content in saline permafrost. To isolate the influences of pore-water salinity, we first made measurements on coarse sand samples for which surface effects are largely negligible. Then, to examine the influences of surface effects in the presence of saline pore water, we also carried out measurements on a fine-grained saline permafrost core sample (extracted from the Barrow Peninsula on the Alaskan Arctic Coastal Plain), in which the silt and clay particle size fractions could yield pronounced surface effects that impact freeze/thaw behavior.

Saturated, coarse-grained Ottawa sand

Standard 20–30 Ottawa sand (quartz; graded between No. 20 and No. 30 sieves, grain size 600–850 μm , D_{50} approximately 720 μm) was used to make fully saturated sand packs. Five saline sand samples, each saturated with an NaCl solution of desired salinity, were used in five individual tests that targeted various levels of pore-water salinities. The salinities of the five NaCl solutions were chosen to represent brackish (0.1 M [6 ppt] and 0.3 M [17 ppt], lower salinity than seawater), moderately saline (0.6 M [35 ppt], typical salinity of seawater), and hypersaline (1.0 M [55 ppt] and 2.5 M [130 ppt], higher salinity than seawater) permafrost. In addition, a nonsaline sample (saturated with distilled water) was used as a baseline for contrasting the results in the presence and absence of dissolved salts. The initial porosity of the saturated sand packs was approximately 36%.

Saturated, fine-grained saline permafrost core sample

The fine-grained saline permafrost core sample used in our experiment was extracted from the Barrow Peninsula on the Alaskan Arctic Coastal Plain. It was the bottom section (depth 1.85–2.80 m) of a 3 m long permafrost core. At the time of coring, the *in situ* ground temperatures were as low as -10°C to -8°C , but this bottom section was only partially frozen because of its saline pore water.

To prevent complications related to heterogeneity and sample saturation state, the core sample was processed via resaturation,

homogenization, repacking, and vacuum de-air steps. The core sample was first thawed in a 4°C refrigerator. From the fully thawed sample, a small amount of the pore water was extracted using a Rhizon soil moisture sampler. The electric conductivity of the extracted pore water was measured (62.3 mS/cm), and an NaCl solution with matching conductivity was prepared. Next, a small amount of this solution was mixed into the thawed core sample for resaturation. After thoroughly homogenizing the mixture by stirring, the sample was packed into the column by adding a small amount each time, followed by mechanical compaction with a plastic rod. Finally, a vacuum was applied to the sample to remove any residual air. After repacking, the electric conductivity of the pore water was measured to be 69.6 mS/cm. Assuming that NaCl is the predominant salt, this conductivity value is equivalent to a salinity of 0.7 M (42 ppt; slightly higher than typical salinity of seawater). The initial porosity of the repacked core sample was approximately 50%.

The combined results of the particle size analysis and X-ray powder diffraction (XRPD) of the homogenized core sample put it in the category of silty-clayey sand (D_{50} approximately 53 μm) consisting of (by volume) 52% sand, 30% silt, and 18% clay (information about the texture analysis is detailed in Appendix A).

Experimental procedure

Temperature control and monitoring

The column was placed inside a bench-top freezer containing a built-in temperature controller. In each set of measurements, the freezer temperature was changed between 10°C and −30°C. The rates of the temperature change were kept slow (1°C every 2–4 h) so that the sample approached a uniform temperature distribution. Sample and freezer temperatures were continuously recorded using a high-resolution data logger (Agilent 34970A) at five-minute intervals.

Ultrasonic data acquisition

A computer-controlled oscilloscope was programmed to continuously acquire P-wave signals at 10 minute intervals. To increase the S/N of the acquired signals via waveform stacking, a pulse generator was tuned to generate trigger pulses with a high repetition rate (100 pulses per second), which enabled a high stack count (128 vertical stacks). Each poststack waveform was recorded by the oscilloscope at a sampling rate of 10 ns over a duration time of 75 μs .

Freeze-only and freeze-thaw measurements

The measurements were conducted under freeze-only or freeze-thaw conditions. For the freeze-only measurements, P-wave signals were acquired only when the sample underwent freezing (i.e., the sample temperatures were decreased from 10°C to −30°C). For the freeze-thaw measurements, P-wave signals were acquired while the sample was going through a freeze-thaw cycle (i.e., the sample temperatures were decreased and then increased between 10°C and −30°C). The main objective of conducting the freeze-thaw measurements is to examine the presence and characteristics of the freeze-thaw hysteresis. We note that freeze-thaw hysteresis usually is more pronounced for fine-grained sediments (Nakano and Froula, 1973). Hence, we conducted freeze-thaw measurements on the fine-grained saline core sample. For the five

coarse sand samples, we only conducted freeze-thaw measurements on one of them (the sample with an initial pore-water salinity of 2.5 M [130 ppt]). Given that no noticeable hysteresis was observed, we conducted freeze-only measurements on the rest of the coarse sand samples.

RESULTS

Here, we present the results of our laboratory ultrasonic measurements as functions of temperature. We first focus on the results of the freezing measurements, which consist of the freeze-only measurements and the freezing subset of the freeze-thaw measurements. We organize these results into three subsections, each corresponding to one of the key factors that control the behavior of the data: (1) the progressions of the water-to-ice phase transitions, (2) the salinities of the pore water, and (3) the presence of fine-grained particles. Near the end of this section, as part of the analysis centering around the effects of grain size — in particular, the influences of the surface effects in the fine-grained saline permafrost core sample — we move on to analyzing the results of the freeze-thaw measurements, in which we use the behavior of the freeze-thaw hystereses as an indicator of the surface effects. Examples shown in this section are for the top sensor pair due to the high degree of uniformity shown between the two measurement locations.

The influences of water-to-ice phase transitions

As the temperatures of the samples gradually dropped below freezing, the freezing resulted in marked changes in the acquired P-wave signals. These changes, while being unique to each sample, exhibit shared features that are correlated with the physical states of the pore water/ice. In this subsection, we use P-wave signals obtained from one of the saline coarse sand samples (initial pore-water salinity = 0.6 M) as examples to demonstrate the influences of the water-to-ice phase transitions.

As can be seen in Figure 6, the temperature-dependent variations of the signal amplitudes (the waveforms and the spectra) can be divided into three distinct segments, each corresponding to a specific state of the sample: (1) the intermediate amplitudes correspond to the unfrozen state (from 10.0°C to −2.0°C), (2) the low amplitudes correspond to the partially frozen state (from −2.0°C to −22.2°C), and (3) the high amplitudes correspond to the fully frozen state (colder than −22.2°C). The boundaries between the adjacent segments are sharp, which results from a rapid decrease and increase of the amplitudes near the freezing point (−2.0°C) and the eutectic point (−22.2°C), respectively.

Figure 7 shows a subset of traces to provide a more detailed view of waveform shape and spectral content. When the temperatures are above freezing, the signals are nearly unresponsive to the temperature changes (7.0°C and −1.0°C in Figure 7). Once the temperatures fall below freezing, the signal shapes become distinctly different at different temperatures. The first cycle of the waveform arrives at successively earlier times as the temperature decreases, illustrating the monotonic increases in the P-wave velocities. By contrast, the associated changes in the spectral contents do not show such monotonicity. Instead, the high-frequency contents of the spectra first diminish at temperatures that are immediately below the freezing point (e.g., −2.3°C and −3.5°C in Figure 7), and then they gradually grow back as the temperatures decrease further (e.g.,

−12.6°C in Figure 7). In the end, when the temperatures are below the eutectic point (e.g., −25.6°C in Figure 7) the waveforms become impulsive and compact, and the spectra include a considerable amount of higher frequencies.

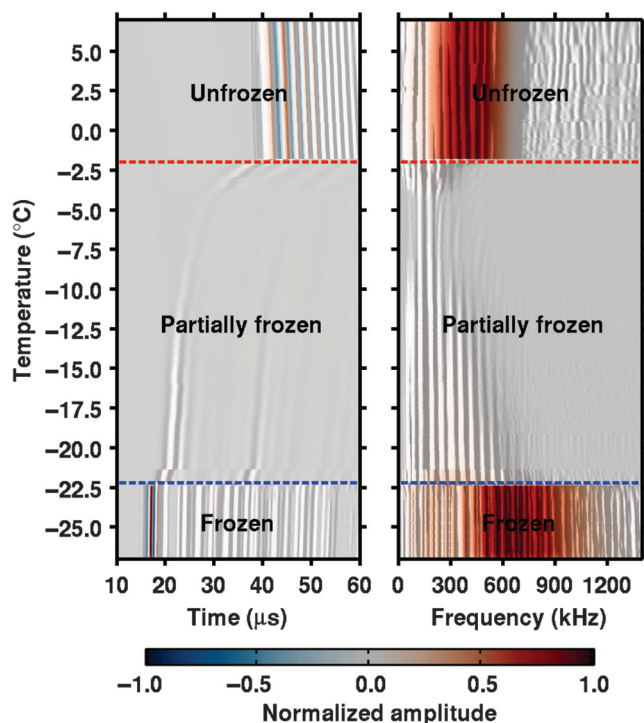


Figure 6. The evolution of (a) the P-wave waveforms and (b) the corresponding amplitude spectra over the course of a freeze-only measurement conducted on one of the saline coarse-sand samples (initial pore-water salinity = 0.6 M [35 ppt]). The relative amplitudes of the signals are preserved.

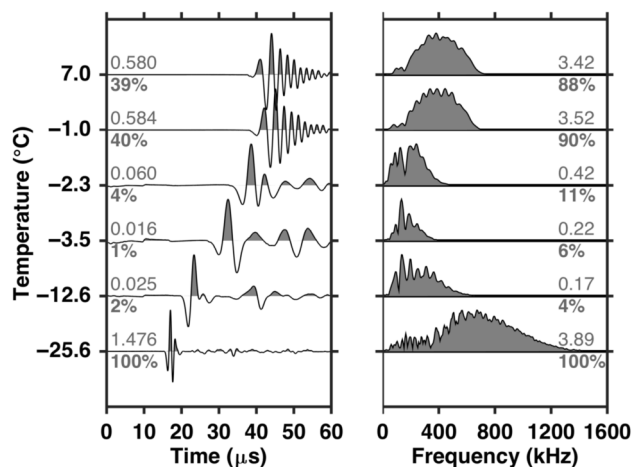


Figure 7. A subset of (a) the normalized P-wave waveforms and (b) the corresponding amplitude spectra extracted from a freeze-only measurement conducted on one of the saline coarse sand samples (initial pore-water salinity = 0.6 M [35 ppt]). On each trace, the numeric value written in gray denotes its maximum amplitude measured in volts; the corresponding percentage value written in gray is relative to the amplitude measured from the fully frozen sample (i.e., $T = -25.6^{\circ}\text{C}$).

The influences of pore-water salinity

Dissolved salts not only lower the freezing point of pore water, but also change how the amount of ice varies with respect to sub-freezing temperatures. As a result, P-wave properties of the samples respond strongly to the presence of dissolved salts. To systematically examine the influences of pore-water salinities, we combine all the data obtained from the six coarse sand samples (five saline

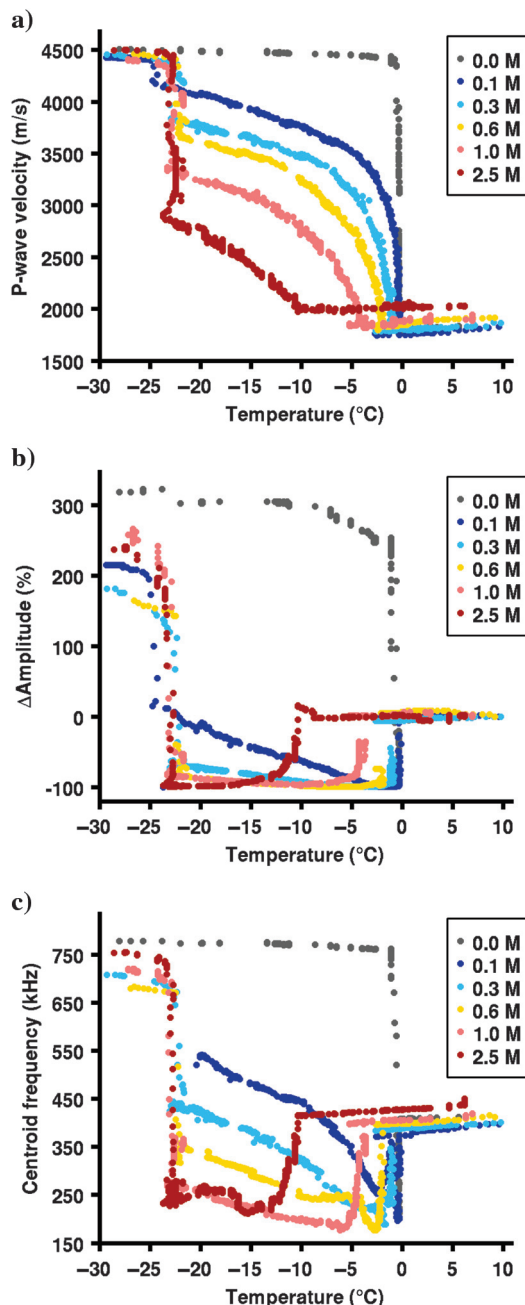


Figure 8. Temperature-dependent variations of P-wave properties obtained from the freezing measurements of saturated 20–30 Ottawa sand: (a) P-wave velocities, (b) relative peak-to-peak amplitudes (relative to the peak-to-peak amplitudes observed at 10°C), and (c) centroid frequencies.

samples and one nonsaline sample) and present them as functions of temperature and initial pore-water salinity (Figure 8).

We first look at the data obtained from the saline samples, for which the freezing process consists of two stages. The first stage starts at the freezing point and ends at the eutectic point. This stage is progressive because the dissolved salts remain in the residual pore water and thus further depress the freezing point. As a result, this stage is characterized by a persistent presence of free water. The second stage corresponds to temperatures that are immediately below the eutectic point. This stage is rapid because the salts quickly precipitate out of the residual pore water and thus can no longer suppress freezing. Once this stage reaches equilibrium, the sample no longer contains free water and is identified as being fully frozen.

To examine the characteristics of this two-stage freezing and compare the behaviors of the data between before and after freezing, we use two reference temperatures, 0°C (the freezing point of water) and −21.3°C (the eutectic point of NaCl aqueous solution), as dividers to break down the results into three parts, each of which corresponds to a distinct stage of the cooling process:

- 1) At warmer than 0°C, all of the samples were unfrozen and thus were equivalent to binary mixtures of sediment grains and brine. In spite of the large differences in the initial pore-water salinities, the observed P-wave properties are largely similar among all the samples. The small intrasample variations and intersample differences in the data can be attributed to the temperature- and salinity-dependent properties (i.e., compressibility, density, and viscosity) of the pore water. Overall, at this stage, the temperature-dependent variations of the P-wave properties are only slightly sensitive to the initial pore-water salinities.
- 2) Between −21.3°C and 0°C, the samples entered their first stage of freezing. The temperature-dependent behaviors of the P-wave properties exhibit large intersample differences as a result of the different initial pore-water salinities. The onset of freezing, marked by rapid rises of the velocities and sudden drops of the amplitudes and the centroid frequencies, occurs at lower temperatures for samples with higher initial salinities, illustrating the positive correlation between the extent of freezing-point depression and the initial pore-water salinity. As freezing progresses further at subfreezing temperatures, the data continue to exhibit temperature-dependent changes that are unique for each sample. In short, at this stage, the temperature-dependent variations of P-wave properties appear to be dictated by the initial pore-water salinities.
- 3) At colder than −21.3°C, the salts rapidly precipitated out of the residual pore water. Upon the loss of the dissolved salts, the second stage of freezing sets in and all the saline samples quickly became fully frozen. The onsets of freezing are marked by abrupt increases in the velocities, amplitudes, and centroid frequencies that occur immediately at colder than −21.3°C. As freezing progresses further at subeutectic temperatures, P-wave properties of all the samples soon converge toward narrow ranges, regardless of the different initial pore-water salinities. Such convergence indicates that the fully frozen samples resemble binary mixtures of sediment grains and ice. The precipitated salts, albeit being visible in the saline samples by the end of the freezing measurements, are too dilute to affect the P-wave properties. Hence, at this stage, the temperature-dependent variations of P-wave properties are largely independent of the initial pore-water salinities.

Next, we bring attention to the striking behavior of amplitudes and centroid frequency during the freezing process (Figure 8b). Once the temperatures fall below freezing, the amplitudes and the centroid frequencies plunge, quickly reaching their minima within another temperature reduction of no more than 5°C. As the temperatures decrease further, the amplitudes and the centroid frequencies slowly rebound but the increase is limited before the second stage of freezing starts. As a result, the amplitudes and centroid frequencies remain low throughout the first stage of freezing, illustrating the presence of strong attenuation in the partially frozen saline samples. Interestingly, the attenuation signatures of the freezing onsets are different between the two stages. Whereas the onset of the first stage of freezing is accompanied by a sharp increase in the attenuation occurring immediately below the freezing point, the second stage of freezing starts with a rapid decline in attenuation near the eutectic point. This near-eutectic behavior of the attenuation is different from what was reported in the studies of Spetzler and Anderson (1968) and Prasad and Dvorkin (2004), both of which examined the seismic attenuation of partially frozen brine and observed increased attenuation near the eutectic point. Such a discrepancy may be related to the microstructural differences between the freezing of unconfined brine and the freezing of saline pore water.

Another curious phenomenon regarding the observed attenuation is that its sharp increase near the freezing point coincides with the rapid rise of the velocity. Such behavior of the data appears counterintuitive, given that increasing velocities often are accompanied by decreasing attenuation. In later parts of this paper, we will revisit the characteristics of the attenuation and expand the related discussion.

Finally, we highlight the influence of the dissolved salts on P-wave properties, which is demonstrated by the drastic differences between the data obtained from the saline and nonsaline samples. It is particularly remarkable that even a small amount of dissolved salts can severely reduce the P-wave velocities. For instance, for the sample with an initial pore-water salinity of a mere 0.1 M (1/6 of the typical seawater salinity), P-wave velocities are up to 12%–36% lower than those of the nonsaline sample in the temperature range from −15°C to −1°C (Figure 8a).

The influences of fine-grained particles

On freezing measurements

Figure 9 compares the data obtained from the freezing measurements conducted on the fine-grained saline permafrost core sample (0.7 M; 42 ppt) against those of the coarse sand samples with neighboring pore-water salinities (0.6 and 1.0 M; 35 and 55 ppt). Because the salinity of the core sample is close enough to those of the two coarse sand samples, the influences of the dissolved salts should be comparable among all three data sets that are being compared here. In this way, the dissimilar behaviors of the data should help to illuminate the influences of the grain-size differences.

As can be seen in Figure 9, the onset of the first stage of freezing, which is marked by a rapid rise in the velocities and sudden drops in the amplitudes and the centroid frequencies, occurs at −2.4°C — a temperature that is consistent with the expected freezing point for an initial pore-water salinity of 0.7 M (42 ppt). Because the freezing point does not appear to be further lowered by the surface effects of the fine-grained particles, we conclude that the influences of the dissolved salts are predominant at near-freezing temperatures.

Throughout the first stage of freezing (from -2.4°C to -21.3°C), P-wave velocities measured from the fine-grained core sample exhibit temperature-dependent variations that are similar to those of the coarse sand samples (Figure 7a), indicating that the dissolved salts exert similar extent of influences on the data regardless of the grain-size differences. In addition, the amplitudes and the centroid frequencies are also markedly lower than the values associated with

the nearly fully frozen stage of the sample (at temperatures that are less than -32°C), illustrating the presence of strong attenuation in the partially frozen saline core sample.

However, the influences of the smaller particle/pore size are also evident, as can be seen from the dissimilar behaviors of the data. For the fine-grained core sample, the onset of the second stage of freezing only becomes identifiable at -31.8°C — a temperature that is well below the expected eutectic point (-21.3°C). Moreover, in contrast with the data from the coarse sand samples that exhibit stepwise variations with respect to near-eutectic temperatures, the data of the core sample show gradual, rampwise changes following the onset of the second stage of freezing, illustrating the influences of the surface effects. P-wave velocities corresponding to the unfrozen and nearly fully frozen stages of the core sample are also lower than those of the coarse sand samples. A simple calculation of the Hashin-Shtrikman-Hill average suggests that the porosity difference between these two samples (approximately 50% for the core sample versus approximately 36% for the sand sample) is the main cause of this discrepancy.

Throughout the first stage of freezing, the temperature-dependent variations of the amplitudes and the centroid frequencies measured from the core sample are noticeably different from those of the coarse sand samples. First, despite that the amplitudes and the centroid frequencies both decrease and then rebound, such as what was observed during the coarse sand experiments, the range of the variations is much smaller. Second, whereas the amplitudes measured from the coarse sand samples rebound very slowly after having reached the minima, the amplitudes measured from the core sample first rebound rapidly within an additional 2°C of temperature drop. After exhibiting a small “bump” (a slight increase followed by a small decrease), the amplitudes continue to slowly increase with decreasing temperatures. These differences could be attributable to the differences in the pore-scale structures, which are closely related to particle shapes and size distributions.

On freeze-thaw measurements

In Figure 10, we compare the velocity data obtained from the freeze-thaw measurements of the fine-grained saline core and the coarse sand samples (initial pore-water salinity = 2.5 M; 130 ppt).

In the temperature range between the freezing point and the eutectic point, we only see subtle freeze-thaw hystereses in both data sets. Given that neither data set exhibits noticeable supercooling within this temperature range, we rule out supercooling-induced hysteresis and are left with capillary hysteresis. The small extent (nearly negligible) of the hystereses in both data sets suggest that with dissolved salts slowing down the freezing, water contained in large pores takes longer to freeze, whereas most of the water in the capillary pores has yet to take part in the freezing.

At subeutectic temperatures, both data sets exhibit noticeable freeze-thaw hysteresis. Interestingly, the two hystereses have distinctly different shape characteristics: The hysteresis of the core sample spans a wider temperature range (between -31.8°C and -21.3°C ; a span of 10.5°C), and the freezing and thawing directions of the hysteresis are gradual, rampwise, and smooth. By contrast, the hysteresis of the coarse sand sample corresponds to a narrow temperature interval of approximately 1.5°C (between -22.8°C and -21.3°C). The freezing and thawing directions of the hysteresis are steep and stepwise, and discernible temperature oscillations are present in the freezing direction.

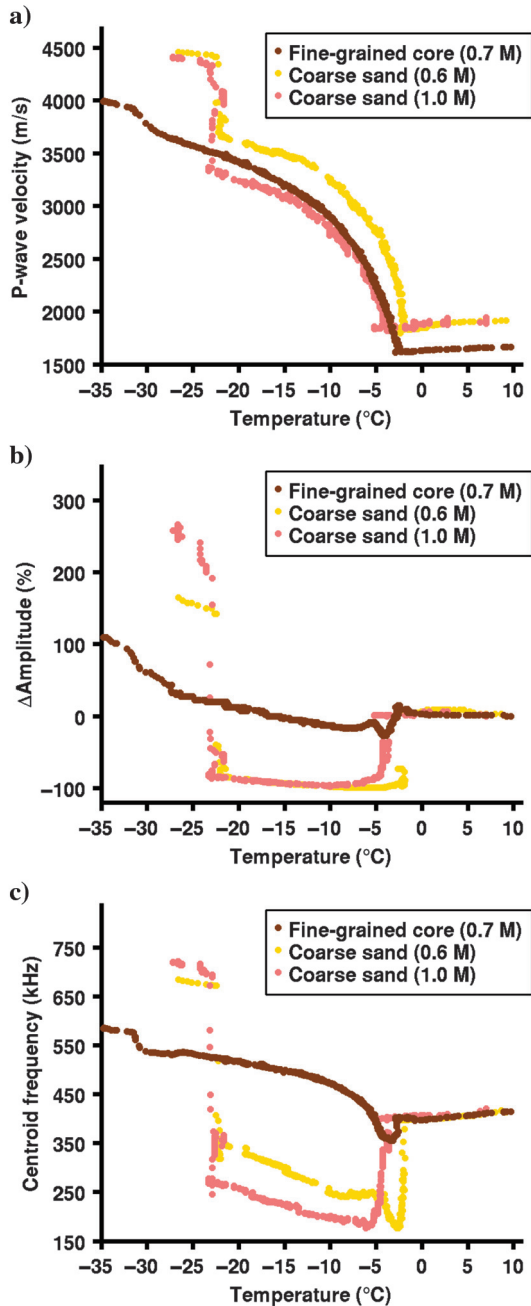


Figure 9. Comparisons of temperature-dependent variations of P-wave properties obtained from the freezing measurements of the fine-grained saline permafrost core sample against those of coarse-grained Ottawa sand with neighboring pore-water salinity: (a) P-wave velocity, (b) relative peak-to-peak amplitudes (relative to peak-to-peak amplitudes observed at 10°C), and (c) centroid frequencies.

The subeutectic hysteresis in these two data sets is governed by different mechanisms. For the fine-grained-core sample, the hysteresis can be explained by the ink-bottle effect shown in Figure 4. For the coarse sand sample, the hysteresis is better explained by supercooling. The temperature oscillation reflects a rapid release of latent heat upon the spontaneous freezing of the supercooled saline pore water (as demonstrated in Figure 3).

DISCUSSION

After having examined the influences of temperatures and salinities, we now consider the relationship between P-wave properties and ice content. As mentioned earlier, although the ice-content variations are the inherent causes of the observed changes in the P-wave properties, what the data directly reveal are the apparent relationships tied to salinities and temperatures. To effectively analyze seismic properties in this context, a mapping is required to estimate ice content from initial pore-water salinities and temperature.

For the water-to-ice phase transitions occurring in the saline pore water, the phase diagram of aqueous NaCl solution is a necessary tool for estimating the ice content. However, this approach is based on the two assumptions: (1) surface effects of the porous media are largely negligible and (2) heterogeneous distributions of dissolved salts, though likely to be present during freezing/thawing of porous media, only have negligible effects on the ice content. In this regard, our saline coarse sand samples provide suitable bases for estimating ice content with the phase diagrams, considering that surface effects in these samples are negligible and the uniform grain/pore sizes are less likely to yield strong salt heterogeneities. Even though these sand samples are simplified representations of the natural saline permafrost, they provide a good entry point for gaining a better understanding of the rock-physics relationship between the ice-content and the P-wave properties.

Ice-content estimation using phase diagrams

We use the phase diagram expressions in Potter et al. (1978) to estimate ice content from initial salinities and temperatures (Figure 11); a more detailed description of the procedure is presented in Appendix B. These expressions allow us to calculate both the freezing point for a given initial salinity and estimate the ice

content for the temperature range from the freezing point to the eutectic point.

Similar expressions have been used in prior studies providing some evidence of applicability in porous media. The Hivon and Sego's (1995) study provides successful precedents of using the phase diagram of NaCl solutions to estimate the unfrozen water content of saline frozen soils. In their study, the estimated values of the unfrozen water content of three different brine-saturated (initial pore-water salinities = 5, 10, and 30 ppt), partially frozen soil samples (sand, D_{50} approximately 400 μm ; silty sand, D_{50} approximately 200 μm ; fine silty sand, D_{50} approximately 80 μm) were compared against the measured values obtained using the time-domain reflectometry method. For all the samples they tested, the two sets of unfrozen-water-content values compare well with each other, suggesting that the phase diagram expressions are applicable to estimate water/ice content of saline frozen sediments.

Ice-content dependencies of P-wave properties

The measured P-wave properties, after being displayed as functions of ice saturation, collapse into tight trends regardless of the initial pore-water salinities as shown in Figure 12. The velocity trends are particularly compact (Figure 12a), illustrating that the changing ice content is the controlling mechanism in the observed velocity variations. The attenuation trends (consisting of the peak-to-peak amplitude and the centroid frequency data) show slightly larger sample-to-sample differences (Figure 12b and 12c). One likely cause of these larger differences is the different viscosities of the residual brine that differ in their salinities (e.g., Matsushima et al., 2013). However, because the data do not exhibit clear salinity-dependent trends, we speculate that in addition to viscosity differences, the microstructures of the samples may also evolve differently, which likely affect attenuation in a different manner and eventually obscure the systematic trends caused by the viscosity differences.

Ice-content dependencies of P-wave velocity

P-wave velocities increase monotonically and steadily with increasing ice saturations (Figure 12a). Although such positive correlations between the velocities and the ice saturations are expected,

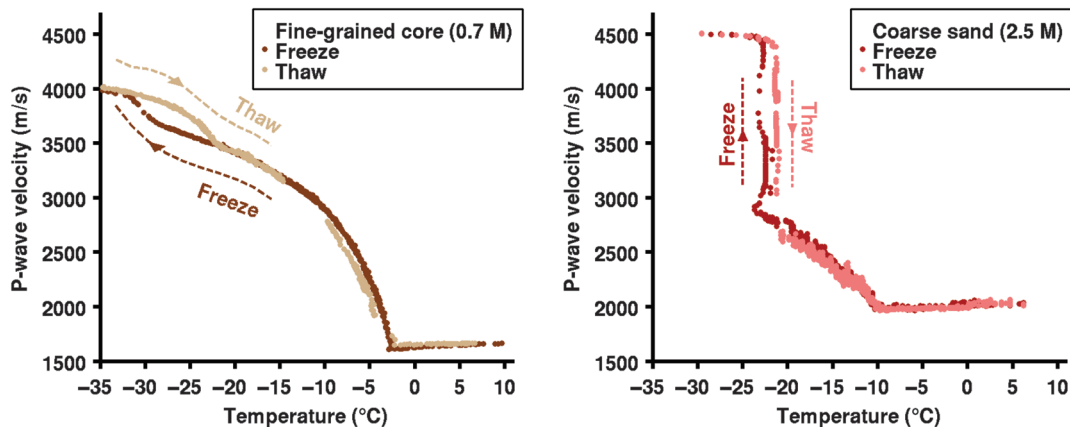


Figure 10. Comparisons of temperature-dependent variations of P-wave velocities between the freeze-thaw measurements of (a) the fine-grained saline permafrost core sample and (b) a brine-saturated coarse sand sample (20–30 Ottawa sand; initial pore-water salinity = 2.5 M [130 ppt]).

the data trend is informative rather than trivial because its shape can give us insight into the growth habits and pore-scale distributions of ice.

Ice-content dependencies of P-wave velocity can take on distinctly different shapes depending upon whether or not the initial growths of ice have preferential affinities to the sediment grains. The curves shown in Figure 12a correspond to several commonly used models that depict end-member scenarios of the pore-scale distributions of ice (Dvorkin et al., 1994, 1999; Dvorkin and Nur, 1996; Helgerud, 2001) based on contact cement theory. If ice growth begins on the grain surfaces, localized to contacts or coating grains, it can effectively act as a stiffening cement even at small ice contents; the resulting relationship between velocity and ice saturation will exhibit a steep increase at low ice saturations, as shown by curves 1 and 2 in Figure 12a.

Alternatively, if ice begins to grow at some distance away from the grain surfaces, a “pore-filling” distribution, it may yield a smaller impact on frame stiffness. Such pore-filling ice can only lead to slight increases in the elastic moduli of the frozen sediments primarily by increasing the moduli of the pore fluids, hence yielding a gradual increase in the velocities as shown by curve 3 in Figure 12a.

However, as shown in Figure 12a, neither cementation nor the pore-filling model for the pore-scale distributions of ice can explain the shape of our data trend, suggesting that the ice nucleation sites may have no particular affinity or aversion to the grain surfaces. The ice-content dependencies of the velocities, which fall in between the predictions of the cementation and pore-filling models, have important implications for rock-physics modeling; that is, the pore-scale distributions of ice may be partly cementing and partly pore filling. Hence, we may need to take into account an intermediate class of ice distributions when constructing rock-physics models for saturated, unconsolidated saline permafrost.

Ice-content dependencies of P-wave attenuation

In contrast to the monotonic increase in the velocities, the P-wave attenuation first increases and then decreases with increasing ice saturations, which results in a trough distribution as can be seen

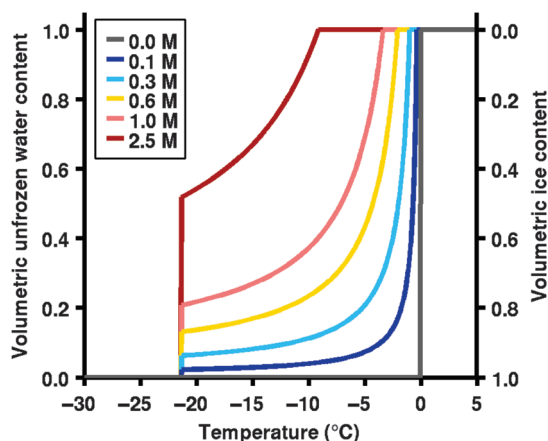


Figure 11. Volume fractions of unfrozen water and ice content (volumetric ice content = 1 — volumetric water content) estimated based on the phase diagram expressions of aqueous NaCl solution in Potter et al. (1978) (Appendix B).

in Figure 12a and 12b. As mentioned earlier, the increase in attenuation is unexpected, given that attenuation typically trends lower in materials with higher velocities. A striking feature of the attenuation curves is the presence of an absorption peak at an ice saturation of approximately 70% (as shown by the converging minima of the amplitudes in Figure 12b). This particular level of ice saturation could be related to a characteristic scale within the samples. Several hypotheses exist to explain the attenuation observations but at this

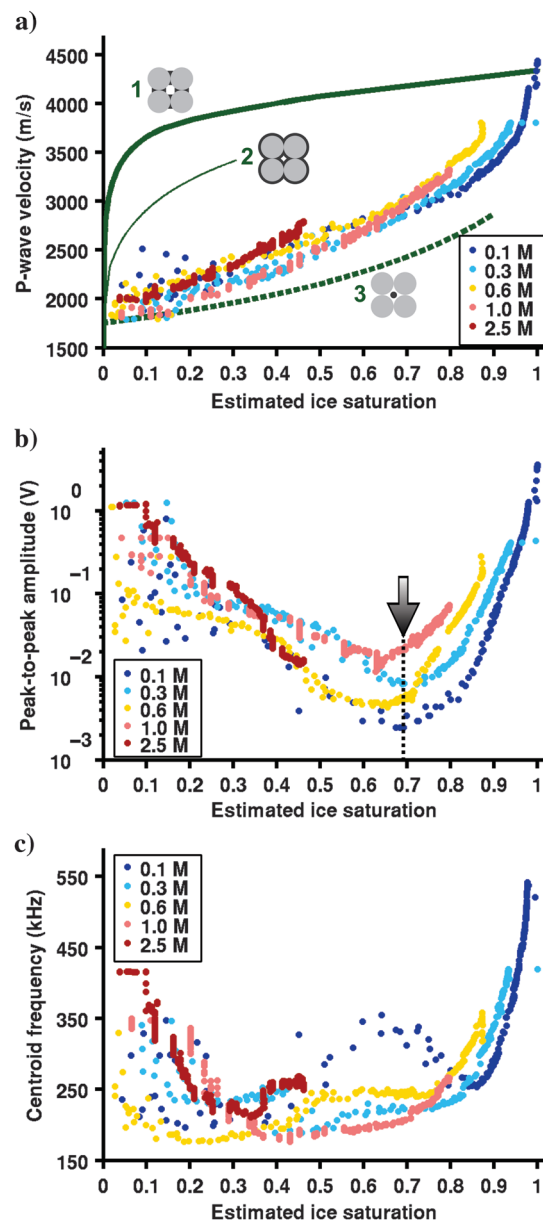


Figure 12. P-wave properties of brine-saturated coarse sand presented as functions of the estimated ice saturation: (a) P-wave velocity, (b) peak-to-peak amplitudes, and (c) centroid frequencies. The green curves in (a) correspond to model-predicted P-wave velocities for three end-member rock-physics models: 1, the stiffest cementation model, in which ice occurs and cements at grain contacts; 2, the second stiffest cementation model, in which ice coats and cements grains; and 3, the softest pore-filling model, in which ice floats in pore space.

point they should be viewed as speculative and include the following:

- 1) Wave-induced phase transition: In a partially frozen medium, ice and water coexist in a delicate equilibrium. This metastable state could easily be disturbed by a small amount of wave energy passing through the medium, causing the proportion of ice and water to oscillate around the equilibrium value. Such phase fluctuations could absorb energy from the wave, yielding intrinsic attenuation. In this case, the characteristic length scale may be related to the wave period that is on the order of or shorter than the relaxation time of the phase fluctuations (Spetzler and Anderson, 1968; Povey, 1997), which could be potentially controlled by either diffusion times or crystallization kinetics.
- 2) Wave-induced fluid flow: When solid and liquid phases coexist in a medium, a passing wave can create pressure gradients, causing the liquid to move relative to the solid. Internal frictions created by this relative motion can lead to intrinsic attenuation of the wave energy. In this case, the characteristic length scale should be comparable to the spatial scale of the pressure gradient (e.g., wavelength-scale Biot attenuation; pore-scale “s squirt” attenuation; and intermediate, mesoscopic-flow-induced attenuation) (Müller et al., 2010).
- 3) Elastic scattering: A partially frozen medium is highly heterogeneous. When the scale of the heterogeneities is comparable to the wavelength, elastic energy can be strongly scattered and redistributed into directions that are away from the direct propagation path between the source and the receiver, resulting in apparent attenuation of the wave energy. In this case, the characteristic scale should be related to the size of the scatterers.

For the attenuation observed in our partially frozen samples, the factors listed above may all have made some contributions. However, because it is difficult to examine the effects of each of these factors separately, the search for the predominant attenuation mechanism is a nontrivial task that is an area of active research (e.g., Carcione et al., 2007; Matsushima et al., 2011a). An in-depth discussion on this topic, however, is beyond the scope of this study.

Although much is yet to be learned before we can fully understand the ice-content dependencies of the attenuation, high P-wave attenuation values seem to be an excellent diagnostic indicator of partially frozen saline permafrost.

CONCLUSIONS

To summarize, through our laboratory ultrasonic measurements, we have produced a rich data set for exploring how P-wave properties vary with respect to temperatures and salinities in saturated, unconsolidated saline permafrost. Moreover, this data set also enabled us to investigate the ice-content dependencies of the P-wave properties that lie in the heart of the rock-physics relationships.

The temperature- and salinity-dependent variations of P-wave properties manifest marked velocity reductions in the presence of dissolved salts and complex variations resulting from the water-to-ice phase transitions. Given the pervasive presence of saline permafrost in subsea and coastal areas of the Arctic, this improved understanding of seismic response should prove useful in subsurface mapping of such zones and monitoring destabilization of permafrost in warming environments.

The ice-content dependencies of P-wave properties show that although the velocities increase monotonically with increasing ice saturations, the attenuation is the highest in the partially frozen state. The velocity data, which cannot be explained by either a purely cementing or a pore-filling model of ice distribution, indicate that the initial growths of ice may have no particular affinity or aversion to grain surfaces. The unexpected presence of strong attenuation, though yet to be fully understood, opens the possibility of incorporating seismic attenuation as a diagnostic tool for detecting and delineating saline permafrost. To move forward, it is crucial to develop rock-physics models that will allow us to quantitatively estimate the ice content from the seismic measurables, given the central role of ice content in mapping present-day distributions and in predicting future responses of saline permafrost.

ACKNOWLEDGMENTS

As part of the Next-Generation Ecosystem Experiments-Arctic (NGEE-Arctic) project sponsored by the Office of Biological and Environmental Research in the DOE Office of Science, this study was supported through contract DEAC0205CH11231 to the Lawrence Berkeley National Laboratory and through contract DE-AC05-00OR22725 to the Oak Ridge National Laboratory. We would like to thank S. Hubbard (Lawrence Berkeley National Laboratory) and S. Wulschleger (Oak Ridge National Laboratory) for their leadership within the NGEE-Arctic program. T. Teague (University of California, Berkeley) and M. Voltolini (Lawrence Berkeley National Laboratory) assisted in conducting XRPD analysis of the permafrost core sample. M. Robertson, P. Cook, and J. Erspamer (all from Lawrence Berkeley National Laboratory) provided substantial assistance in setting up the measurement system. Last but not least, we would like to thank the three reviewers — D. Schmitt, M. Prasad, one anonymous reviewer — and the associate editor J. Bradford for their constructive reviews and comments.

APPENDIX A

TEXTURE INFORMATION OF THE SALINE PERMAFROST CORE SAMPLE

The texture of the saline permafrost core sample was first measured with a laser diffraction particle size analyzer (Malvern Mastersizer 3000). Because the amount of clay was not well constrained using the laser diffraction sizing technique alone, the texture information was then refined based on the mineral composition measurements obtained through XRPD analysis. The results of this two-step procedure (detailed in Table A-1) determined that the core sample is a silty-clayey sand (D_{50} approximately 53 μm) consisting of 52 vol % sand, 30 vol % silt, and 18 vol % clay.

APPENDIX B

VOLUME FRACTIONS OF ICE AND WATER

For a given initial (i.e., prior to freezing) pore-water salinity S_{n0} (in wt%), the corresponding freezing point T_{fp} (in $^{\circ}\text{C}$) is (Potter et al., 1978) as follows:

$$T_{fp} = 0.00 - (0.581855S_{n0} + 3.48896 \times 10^{-3}S_{n0}^2 + 4.314 \times 10^{-4}S_{n0}^3). \quad (\text{B-1})$$

Table A-1. Texture information of the saline permafrost core sample.

Method	Results	Vol%
Laser diffraction particle size analysis	Particle types	
	Medium sand (250–500 μm)	1.5
	Fine to very fine sand (50–250 μm)	50.5
	Subsand fines (<50 μm , silt- and clay-sized particles)	48
XRPD analysis	Mineral types	
	Quartz	68
	Plagioclase	11
	Clay minerals (kaolinite and chloride)	18
	Secondary minerals (dolomite, muscovite, and halite)	3
Combination	Texture classes	
	Sand	52
	Silt	30
	Clay	18

For a given subfreezing temperature T ($T < T_{fp}$; in $^{\circ}\text{C}$), the minimum salinity S_n (in wt%) required to prevent the residual pore water from freezing is (Potter et al., 1978) as follows:

$$S_n = 1.76958|T| - 4.2384 \times 10^{-2}|T|^2 + 5.2778 \times 10^{-4}|T|^3. \quad (\text{B-2})$$

Assuming that in the temperature range between the freezing point T_{fp} (in $^{\circ}\text{C}$) and the eutectic point $T_{eutectic}$ (in $^{\circ}\text{C}$), the total mass of the dissolved salts $m_{\text{salt}}^{\text{total}}$ remains constant in the residual pore water. Then, by denoting the initial mass of the pore water at above-freezing temperatures as m_{w0} and the mass of the residual pore water at subfreezing temperatures as m_w , the mass conservation of the dissolved salts yields

$$m_{\text{salt}}^{\text{total}} = S_{n0}m_{w0} = S_n m_w. \quad (\text{B-3})$$

Given that $m_{w0} = \rho_{w0}V_{w0}$ and $m_w = \rho_w V_w$, equation B-3 can be rewritten as follows:

$$S_{n0}\rho_{w0}V_{w0} = S_n\rho_w V_w, \quad (\text{B-4})$$

where ρ_w and V_w are the density and volume of the saline pore water, respectively, and their initial values are $\rho_{w0} = \rho_w|_{S_n=S_{n0}, T=T_0}$ and $V_{w0} = V_w|_{S_n=S_{n0}, T=T_0}$. In saline permafrost, the initial volume of water V_{w0} equals to the total volume of the pore space $V_{\text{pore}}^{\text{total}}$ ($V_{w0} = V_{\text{pore}}^{\text{total}}$). After reorganizing equation B-4, the unfrozen water saturation S_w ($S_w = V_w/V_{\text{pore}}^{\text{total}}$, the volume fraction of residual unfrozen water in the pore space; unitless fraction) and ice saturation S_i ($S_i = V_i/V_{\text{pore}}^{\text{total}}$, the volume fraction of ice in the pore space; unitless fraction) can be expressed as follows:

$$S_w = \frac{V_w}{V_{\text{pore}}^{\text{total}}} = \frac{V_w}{V_{w0}} = \frac{\rho_{w0}S_{n0}}{\rho_w S_n},$$

$$S_i = \frac{V_i}{V_{\text{pore}}^{\text{total}}} = \frac{V_{\text{pore}}^{\text{total}} - V_w}{V_{\text{pore}}^{\text{total}}} = 1 - \frac{V_w}{V_{\text{pore}}^{\text{total}}} = 1 - S_w. \quad (\text{B-5})$$

If the initial pore-water salinity S_{n0} and the temperatures T are known, the salinities of the residual pore water S_n during freezing are given by equation B-2, and the pore-water densities ρ_w and ρ_{w0} can be obtained based on the Batzle and Wang's (1992) study. Then, the unfrozen S_w and S_i of saline permafrost can be estimated using equation B-5 within the temperature range of $T_{\text{eutectic}} \leq T \leq T_{fp}$.

REFERENCES

- Andersland, O. B., and B. Ladanyi, 2004, *Frozen ground engineering*, 2nd ed.: Wiley, American Society of Civil Engineers.
- Anderson, R., B. Tohidi, and J. B. W. Webber, 2009, Gas hydrate growth and dissociation in narrow pore networks: Capillary inhibition and hysteresis phenomena: Geological Society of London, Special Publications, **319**, 145–159, doi: [10.1144/SP319.12](https://doi.org/10.1144/SP319.12).
- Batzle, M., and Z. Wang, 1992, Seismic properties of pore fluids: *Geophysics*, **57**, 1396–1408, doi: [10.1190/1.1443207](https://doi.org/10.1190/1.1443207).
- Bittelli, M., M. Flury, and G. S. Campbell, 2003, A thermoelectric analyzer to measure the freezing and moisture characteristic of porous media: *Water Resources Research*, **39**, 1041, doi: [10.1029/2001WR000930](https://doi.org/10.1029/2001WR000930).
- Blachere, J. R., and J. E. Young, 1972, The freezing point of water in porous glass: *Journal of the American Ceramic Society*, **55**, 306–308, doi: [10.1111/j.1151-2916.1972.tb11291.x](https://doi.org/10.1111/j.1151-2916.1972.tb11291.x).
- Brouchkov, A., 2002, Nature and distribution of frozen saline sediments on the Russian Arctic coast: *Permafrost and Periglacial Processes*, **13**, 83–90, doi: [10.1002/ppp.411](https://doi.org/10.1002/ppp.411).
- Brouchkov, A., 2003, Frozen saline soils of the Arctic coast: Their distribution and engineering properties: *Proceedings of the 8th International Conference on Permafrost*, National Academy of Sciences.
- Carcione, J. M., O. H. Campanella, and J. E. Santos, 2007, A poroelastic model for wave propagation in partially frozen orange juice: *Journal of Food Engineering*, **80**, 11–17, doi: [10.1016/j.jfoodeng.2006.04.044](https://doi.org/10.1016/j.jfoodeng.2006.04.044).
- Collett, T. S., and K. J. Bird, 1988, Freezing-point depression at the base of the ice-bearing permafrost on the North Slope of Alaska: *Proceedings of the 5th International Conference on Permafrost*, Tapir Publishers.
- Collett, T. S., and K. J. Bird, 1993, Unfrozen, high-salinity intervals within ice-bearing permafrost, North Slope of Alaska: *Proceedings of the 6th International Conference on Permafrost*, South China University of Technology Press.
- Davis, T. N., 2001, *Permafrost: A guide to frozen ground in transition*: University of Alaska Press.
- Desai, K. P., and E. J. Moore, 1967, Well log interpretation in permafrost: SPWLA 8th Annual Logging Symposium, Society of Petrophysicists and Well Log Analysts.
- Dou, S., and J. Ajo-Franklin, 2014, Full-wavefield inversion of surface waves for mapping embedded low-velocity zones in permafrost: *Geophysics*, **79**, no. 6, EN107–EN124, doi: [10.1190/geo2013-0427.1](https://doi.org/10.1190/geo2013-0427.1).
- Dvorkin, J., J. Berryman, and A. Nur, 1999, Elastic moduli of cemented sphere packs: *Mechanics of Materials*, **31**, 461–469, doi: [10.1016/S0167-6636\(99\)00009-5](https://doi.org/10.1016/S0167-6636(99)00009-5).
- Dvorkin, J., and A. Nur, 1996, Elasticity of high-porosity sandstones: Theory for two North Sea data sets: *Geophysics*, **61**, 1363–1370, doi: [10.1190/1.1444059](https://doi.org/10.1190/1.1444059).
- Dvorkin, J., A. Nur, and H. Yin, 1994, Effective properties of cemented granular materials: *Mechanics of Materials*, **18**, 351–366, doi: [10.1016/0167-6636\(94\)90044-2](https://doi.org/10.1016/0167-6636(94)90044-2).
- Fagerlund, G., 1973, Determination of pore-size distribution from freezing-point depression: *Matériaux et Construction*, **6**, 215–225, doi: [10.1007/BF02479036](https://doi.org/10.1007/BF02479036).
- Hall, C., and W. D. Hoff, 2012, *Frost damage: Water transport in brick, stone, and concrete*: Spon Press, 277–288.
- Helgerud, M. B., 2001, Wave speeds in gas hydrate and sediments containing gas hydrate: A laboratory and modeling study: Ph.D. dissertation, Stanford University.
- Hilbich, C., 2010, Time-lapse refraction seismic tomography for the detection of ground ice degradation: *The Cryosphere*, **4**, 243–259, doi: [10.5194/tc-4-243-2010](https://doi.org/10.5194/tc-4-243-2010).
- Hivon, E. G., and D. C. Sego, 1993, Distribution of saline permafrost in the Northwest Territories, Canada: *Canadian Geotechnical Journal*, **30**, 506–514, doi: [10.1139/93-043](https://doi.org/10.1139/93-043).

- Hivon, E. G., and D. C. Sego, 1995, Strength of frozen saline soils: Canadian Geotechnical Journal, **32**, 336–354, doi: [10.1139/t95-034](https://doi.org/10.1139/t95-034).
- Ingeman-Nielsen, T., N. N. Foged, and A. S. Jørgensen, 2008, Geophysical investigation of saline permafrost at Ilulissat, Greenland: Proceedings of the 9th International Conference on Permafrost, Institute of Northern Engineering, University of Alaska Fairbanks.
- King, M. S., B. I. Pandit, J. A. Hunter, and M. Gajtani, 1982, Some seismic, electrical, and thermal properties of sub-seabottom permafrost from the Beaufort Sea: Proceedings of the 4th Canadian Permafrost Conference, National Research Council Canada.
- Kofman, R., A. Rabbani, G. Njiekak, and D. R. Schmitt, 2013, Influence of cooling and heating rate on CO₂ condensation and evaporation observed in a saturated synthetic rock sample: GeoConvention.
- Kozłowski, T., and E. Nartowska, 2013, Unfrozen water content in representative bentonites of different origin subjected to cyclic freezing and thawing: Vadose Zone Journal, **12**, doi: [10.2136/vzj2012.0057](https://doi.org/10.2136/vzj2012.0057).
- Matsushima, J., M. Suzuki, Y. Kato, and S. Rokugawa, 2011a, Laboratory measurements of ultrasonic P-wave and S-wave attenuation in partially frozen unconsolidated sediments saturated with brine: 81st Annual International Meeting, SEG, Expanded Abstracts, 2130–2134.
- Matsushima, J., M. Suzuki, Y. Kato, and S. Rokugawa, 2011b, Estimation of ultrasonic scattering attenuation in partially frozen brines using magnetic resonance images: Geophysics, **76**, no. 1, T13–T25, doi: [10.1190/1.3511355](https://doi.org/10.1190/1.3511355).
- Matsushima, J., M. Suzuki, Y. Kato, and S. Rokugawa, 2013, Effects of viscosity of unfrozen brine in partially frozen unconsolidated sediments on ultrasonic wave attenuation: Proceedings of the 11th SEGJ International Symposium, SEG, 383–386.
- Miller, R. D., J. A. Hunter, W. E. Doll, B. J. Carr, R. A. Burns, R. L. Good, D. R. Laflen, and M. Douma, 2000, Imaging permafrost with shallow P- and S-wave reflection: 70th Annual International Meeting, SEG, Expanded Abstracts, 1339–1342.
- Müller, T., B. Gurevich, and M. Lebedev, 2010, Seismic wave attenuation and dispersion resulting from wave-induced flow in porous rocks — A review: Geophysics, **75**, no. 5, 75A147–175A164, doi: [10.1190/1.3463417](https://doi.org/10.1190/1.3463417).
- Nakano, Y., and R. Arnold, 1973, Acoustic properties of frozen Ottawa sand: Water Resources Research, **9**, 178–184, doi: [10.1029/WR009i001p00178](https://doi.org/10.1029/WR009i001p00178).
- Nakano, Y., and N. H. Froula, 1973, Sound and shock transmission in frozen soils: Proceedings of the 2nd International Conference on Permafrost, National Academy of Sciences.
- Nixon, J. F., and G. Lem, 1984, Creep and strength testing of frozen saline fine-grained soils: Canadian Geotechnical Journal, **21**, 518–529, doi: [10.1139/t84-054](https://doi.org/10.1139/t84-054).
- Ogata, N., M. Yasuda, and T. Kataoka, 1983, Effects of salt concentration on strength and creep behavior of artificially frozen soils: Cold Regions Science and Technology, **8**, 139–153, doi: [10.1016/0165-232X\(83\)90005-8](https://doi.org/10.1016/0165-232X(83)90005-8).
- Osterkamp, T. E., 1989, Occurrence and potential importance of saline permafrost in Alaska: Workshop on Saline Permafrost, University of Manitoba.
- Pandit, B. I., and M. S. King, 1978, Influence of pore fluid salinity on seismic and electrical properties of rocks at permafrost temperatures: Proceedings of International Conference on Permafrost, U.S. National Academy of Sciences.
- Pandit, B. I., and M. S. King, 1979, A study of the effects of pore-water salinity on some physical properties of sedimentary rocks at permafrost temperatures: Canadian Journal of Earth Sciences, **16**, 1566–1580, doi: [10.1139/e79-143](https://doi.org/10.1139/e79-143).
- Potter, R. W., M. A. Clynne, and D. L. Brown, 1978, Freezing point depression of aqueous sodium chloride solutions: Economic Geology, **73**, 284–285, doi: [10.2113/gsecongeo.73.2.284](https://doi.org/10.2113/gsecongeo.73.2.284).
- Povey, M. J. W., 1997, Multiphase media: Ultrasonic techniques for fluids characterization: Academic Press, 47–90.
- Prasad, M., and J. Dvorkin, 2004, Velocity and attenuation of compressional waves in brines: 74th Annual International Meeting, SEG, Expanded Abstracts, 1666–1669.
- Ramachandran, K., G. Bellefleur, T. Brent, M. Riedel, and S. Dallimore, 2011, Imaging permafrost velocity structure using high resolution 3D seismic tomography: Geophysics, **76**, no. 5, B187–B198, doi: [10.1190/geo2010-0353.1](https://doi.org/10.1190/geo2010-0353.1).
- Schmitt, D. R., M. Welz, and C. D. Rokosh, 2005, High-resolution seismic imaging over thick, permafrost at the 2002 Mallik drill site, in S. R. Dallimore, and T. S. Collett, eds., Scientific results from the Mallik 2002 gas hydrate production research well program Mackenzie Delta, Northwest Territories, Canada: Geological Survey of Canada Bulletin 585.
- Schön, J., 2011, Physical properties of rocks: A workbook (Handbook of petroleum exploration and production): Elsevier.
- Setzer, M. J., 1997, Basis of testing the freeze-thaw resistance: Surface and internal deterioration, in R. Auberg, and M. J. Setzer, eds., Frost resistance of concrete: CRC Press, 166–181.
- Sondergeld, C., and C. Rai, 2007, Velocity and resistivity changes during freeze-thaw cycles in Berea sandstone: Geophysics, **72**, no. 2, E99–E105, doi: [10.1190/1.2435198](https://doi.org/10.1190/1.2435198).
- Spaans, E. J. A., and J. M. Baker, 1996, The soil freezing characteristic: Its measurement and similarity to the soil moisture characteristic: Soil Science Society of America Journal, **60**, 13–19, doi: [10.2136/sssaj1996.03615995006000010005x](https://doi.org/10.2136/sssaj1996.03615995006000010005x).
- Spetzler, H., and D. L. Anderson, 1968, The effect of temperature and partial melting on velocity and attenuation in a simple binary system: Journal of Geophysical Research, **73**, no. 18, 6051–6060, doi: [10.1029/JB073i018p06051](https://doi.org/10.1029/JB073i018p06051).
- Timur, A., 1968, Velocity of compressional waves in porous media at permafrost temperatures: Geophysics, **33**, 584–595, doi: [10.1190/1.1439954](https://doi.org/10.1190/1.1439954).
- Wilson, P. W., A. F. Heneghan, and A. D. J. Haymet, 2003, Ice nucleation in nature: Supercooling point (SCP) measurements and the role of heterogeneous nucleation: Cryobiology, **46**, 88–98, doi: [10.1016/S0011-2240\(02\)00182-7](https://doi.org/10.1016/S0011-2240(02)00182-7).
- Zachariassen, K. E., 2005, Freezing and supercooling of water: Water Encyclopedia: John Wiley & Sons Inc.
- Zimmerman, R. W., and M. S. King, 1986, The effect of the extent of freezing on seismic velocities in unconsolidated permafrost: Geophysics, **51**, 1285–1290, doi: [10.1190/1.1442181](https://doi.org/10.1190/1.1442181).